Geochemistry, Geophysics, Geosystems

RESEARCH ARTICLE
10.1029/2019GC008298

Key Points:
- Marine sediment cores from the southwest Iceland-Faroe Ridge reveal prominent sedimentary cycles due to Iceland-Scotland Overflow dynamics
- Variations in grain-size distributions and provenance are tightly coupled following Dansgaard-Oeschger cycles over the last 55-6 ka BP
- Current-controlled sediment deposition reflects the cumulative effect of overflow cascading over the ridge and through the Faroe Channels

Supporting Information:
- Supporting Information S1

Correspondence to:
M. Mirzaloo,
mmirzaloo@geomar.de

Citation:
Mirzaloo, M., Nürnberg, D., Kienast, M., & van der Lubbe, H. J. L. (2019). Synchronous changes in sediment transport and provenance at the Iceland-Faroe Ridge linked to millennial climate variability from 55 to 6 ka BP. *Geochemistry, Geophysics, Geosystems*, *20*, 4184–4201. https://doi.org/10.1029/2019GC008298

Received 28 FEB 2019
Accepted 25 JUL 2019
Accepted article online 30 JUL 2019
Published online 21 AUG 2019

The copyright line for this article was changed on 20 NOV 2019 after original online publication.

©2019. The Authors.
This is an open access article under the terms of the Creative Commons Attribution License, which permits use, distribution and reproduction in any medium, provided the original work is properly cited.

Synchronous Changes in Sediment Transport and Provenance at the Iceland-Faroe Ridge Linked to Millennial Climate Variability From 55 to 6 ka BP

M. Mirzaloo[1], D. Nürnberg[1], M. Kienast[2], and H. J. L. van der Lubbe[3]

[1]Ocean Circulation and Climate Dynamics, GEOMAR Helmholtz Centre for Ocean Research Kiel, Kiel, Germany, [2]Department of Oceanography, Dalhousie University, Halifax, Nova Scotia, Canada, [3]Department of Geology and Geochemistry, Faculty of Science, Vrije Universiteit Amsterdam, Amsterdam, the Netherlands

Abstract Unique marine sediment cores retrieved from the southwestern slope of the Iceland-Faroe Ridge (IFR), close to the main axis of the Iceland-Scotland Overflow Water (ISOW), revealed prominent sedimentary cycles reflecting near-bottom current dynamics, sediment transport, and deposition, coincident with Dansgaard-Oeschger cycles and deglacial perturbations of the Atlantic Meridional Overturning Circulation. The transition between Greenland Stadials (GSs) and Greenland Interstadials (GIs) follows a distinct, recurring sedimentation pattern. Basaltic (Ti-rich) silts were transported from local volcanic sources by strong bottom currents and deposited during GIs comparable to modern ocean circulation. Finer-grained felsic (K-rich) sediments were deposited during GSs, when Iceland-Scotland Overflow was weak. Possible felsic source areas include British-Ireland and/or Fennoscandian shelf areas. A cyclic sawtooth pattern of bottom current strength is characterized by gradual intensification during GIs followed by a sharp decline toward GSs as is documented at core sites along the flank of Reykjanes Ridge. The cores north of the Faroe Channel instead document the opposite pattern. This suggests that the near-bottom currents along the Reykjanes Ridge are strongly controlled by the flow cascading over the IFR. Heinrich-(like) HS-1 and HS-2, are characterized by the deposition of very fine felsic sediments pointing to weakened bottom currents. Distinct coarse-grained intervals of ice-rafted debris are absent from the sediment records, although pebble- and gravel-sized ice-rafted debris is irregularly distributed throughout the fine sediment matrix. Near-bottom currents are considered to have a major control on the lithogenic sediment deposition southwest of the IFR and further downstream.

Plain Language Summary The northward flow of warm North Atlantic water into the Nordic Seas and the southward return of cold and dense overflow water toward the Atlantic basin drive the Atlantic Meridional Overturning Circulation, which is a significant component in the Earth's climate system. Reconstructions of past Atlantic Meridional Overturning Circulation variations are pivotal to our knowledge of the climate response to rapid warming both in the past and the future. The Iceland-Scotland Ridge is an important gateway for southward-directed Iceland-Scotland Overflow Water. Unique marine sedimentary archives from the southwestern slope of the Iceland-Faroe Ridge close to the main axis of Iceland-Scotland Overflow Water were systematically studied for their grain size distributions and chemical composition in order to reconstruct near-bottom circulation dynamics during rapid cooling and warming phases in the northern Atlantic basin. The records reveal marked changes in particle size and provenance, which are clearly related to near-bottom current speed and hence overflow over the Iceland-Scotland Ridge coincident with major abrupt climate change events.

1. Introduction

The Atlantic Meridional Ocean Circulation is a vital component of Earth's climate system, transporting tropical warm and saline surface water masses toward the northern North Atlantic Ocean and thus contributes to a relatively mild climate in northwest Europe (Rahmstorf, 2002). North Atlantic surface water cools along its transit and sinks in the Nordic Seas, before returning as cold and dense overflow water contributing to North Atlantic Deep Water (NADW; Figure 1). An estimated ~6 Sv (1 Sv = 10^6 m^3/s; Hansen & Østerhus, 2000) flow across the shallow volcanic ridge between Greenland and

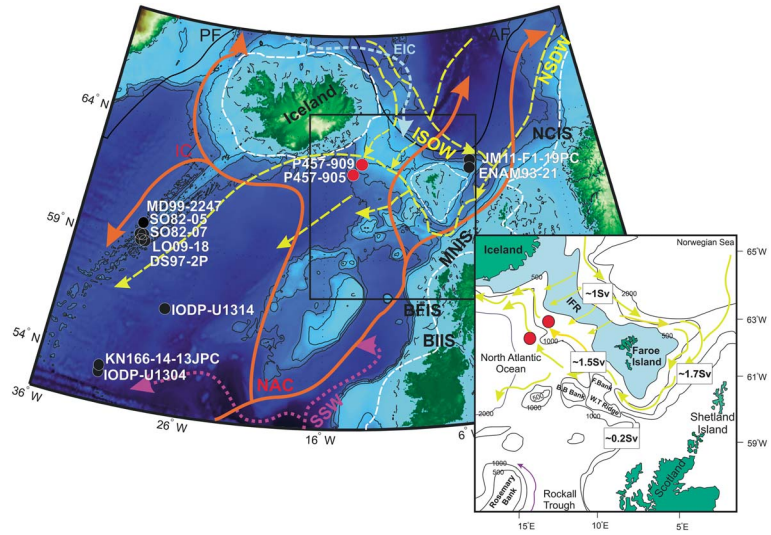

Figure 1. Bathymetric chart of the study area showing the location of studied core sites (red dots) P457-905 (62°41.13′N 14°21.15′W, 1,610-m water depth), P457-909 (62°50.20′N 12°59.47′W, 755-m water depth) and the modern oceanic circulation pattern. Black dots indicate adjacent cores, which are discussed in this study. Red arrows mark the surface circulation of the warm and salty North Atlantic Current (NAC) and the Irminger Current (IC). Dashed yellow arrows denote deep currents carrying Iceland-Scotland Overflow Water (ISOW) and Norwegian Sea Deep Water (NSDW). Dashed light blue arrows show the relatively cold and fresh surface to subsurface East Icelandic Current (EIC). Purple dashed lines show Southern Source Water (SSW). The black lines indicate the present Polar Front (PF), which represents the transition between Polar and Arctic waters, and the Arctic Front (AF). Dashed white lines outline the extension of continental British Ireland Ice Sheet (BIIS) and Norwegian Ice sheet during the LGM. Major ice streams: Bara Fan Ice Stream (BFIS), Minch Ice Stream (MNIS), and Norwegian Channel Ice Stream (NCIS) (Scourse et al., 2009). To the right, the bathymetric map (modified from Hansen & Østerhus, 2000; Ostmann et al., 2014) with contours in meters and a blue shaded area <500 m of the Iceland-Faroe Ridge (IFR), the Faroe-Shetland Channel, and Faroe Bank Channel provides information on the modern near-bottom currents (yellow arrows) and according transport rates (in Sverdrups; 1 Sv = 10^6 m^3/s). Red dots indicate the locations of sediment cores 909 and 905.

Scotland, of which only Iceland and the Faroe Islands emerge above sea level. About half of this return flow (~3 Sv) is routed as Iceland-Scotland Overflow Water (ISOW; Figure 1; Hansen & Østerhus, 2000). This northern limb of the Atlantic Meridional Ocean Circulation has been shown to be intrinsically linked with climate change, shifting its mode of operation frequently during the last glacial period in pace with Greenland Stadials (GSs) and Interstadials (GIs; i.e., Dansgaard-Oeschger [D-O] oscillations; Dokken et al., 2013). Changes in the flow of ISOW have also been observed in concert with more recent, interannual and decadal changes in the North Atlantic Oscillation (Boessenkool et al., 2007). A better understanding of the dynamics of the ISOW in relation to (paleo)climate variability is therefore critically important.

High-resolution atmospheric temperature records derived from Greenland ice cores display distinct D-O oscillations, which are characterized by abrupt warming at the onsets of GIs and gradual cooling toward the GS conditions (North Greenland Ice Core Project, NGRIP). These comparable events are also documented in Antarctic ice cores, although the warming phases are more gradual, less pronounced, and not entirely synchronous with D-O events in Greenland ice cores (Veres et al., 2013). Many paleoproxy records from North Atlantic sediment cores also mimic D-O variability (Ezat et al., 2014; Kissel, 2005; McCave & Hall, 2006; Rasmussen, Thomsen, Weering, & Labeyrie 1996; Rasmussen et al., 1998). Marine sediments that are currently under the pathway of ISOW are likely ideal candidates to reconstruct past changes in the variability of near-bottom circulation patterns and current velocities along the Iceland-Faroe Ridge (IFR), including the thick and extensive deposits (i.e., contourites), which afford a high temporal resolution (Rebesco et al., 2014).

The lithogenic sediment composition monitored by bulk Ti/K ratio and magnetic susceptibility (MS) in sediment cores from northeast of the Faroe Islands varies in close agreement with the D-O oscillations in the Greenland ice cores (Ballini et al., 2006; Hoff et al., 2016; Richter et al., 2006). These records are interpreted to reflect variable sediment provenance in response to either changes in relative contribution of different

sources or varying modes of sediment transport deposition, with local volcanic (Ti-rich, high MS) sediments dominant during warm GIs and distal felsic sources (K-rich, low MS) more prevalent during cold (Heinrich) stadials (Hoff et al., 2016; Richter et al., 2006). Changes in lithogenic grain size distributions have also been used to reconstruct past changes in near-bottom currents across the Icelandic Basin (Ballini et al., 2006; Jonkers et al., 2009; McCave & Andrews, 2019; Prins et al., 2001; Snowball & Moros, 2003; Thornalley, Blaschek, et al., 2013). So far, sediment cores from the IFR have not been systematically investigated for their sediment grain size distributions and provenances in relation to near-bottom current activity, and sediment transport and deposition.

We analyzed the lithogenic grain size composition of two sediment cores (P457-905 and -909) from the southwestern flank of the IFR, north of the main ice-rafted debris (IRD) belt and near the main pathway of ISOW (Werner & Nürnberg, 2014). Complemented by high-resolution records of X-ray fluorescence (XRF) bulk chemistry, weighed coarse bulk fraction (>63 μm), and the isotopic composition of benthic foraminifera shells, these records address near-bottom current and overflow dynamics on glacial to deglacial timescales at centennial to decadal resolution.

2. Modern Oceanographic and Climatic Settings

Overall, ~3 Sv of ISOW flow from the Nordic Seas into the Atlantic Ocean via the IFR, Faroe-Shetland Channel (FSC) and Faroe-Bank Channel (FBC; Figure 1). Approximately 1 Sv is transported via depressions of the shallow IFR with minima of ~300- to 500-m water depth (m wd; Dorn & Werner, 1993). About 1.7 Sv flow through the deep (~1,000-m wd) FSC, of which ~1.5 Sv is directed westward through the FBC (Hansen & Østerhus, 2000). Bottom currents through the FBC together with overflow waters from the shallow IFR form a high-energy near-bottom contour current at water depths between ~600 and 1,000 m along the southwestern flank of the IFR (Dorn & Werner, 1993; Kuijpers & Nielsen, 2016; Kuijpers et al., 1998; Kuijpers et al., 2002). The presence of contour current-induced sand bedforms indicates occasionally very high near-bottom flow velocities with maxima of ~90 cm/s, which likely mark the main axis of ISOW (Dorn & Werner, 1993; Kuijpers et al., 1998).

Float measurements between ~1,500 and 1,000-m wd reveal average speeds of 21 cm/s along the SW flank of the IFR (Beaird et al., 2013), in agreement with flow speeds of 20–30 cm/s measured closer to the FBC (Hansen & Meincke, 1979). Approaching the Icelandic continental shelf, the contour current is deflected in a southwesterly direction (Figure 1). Further to the southwest, flow is reduced to 13 to 21 cm/s at ~2,000–2,300-m wd (McCave et al., 2017). Hereafter, ISOW flows parallel to the axis of Reykjanes Ridge at ~1,200–1,800-m wd, where it interacts with Labrador Sea Water and continues its way to the western Icelandic basin via the Charlie-Gibbs Fracture Zone, contributing to NADW (Bower et al., 2017).

The overflow is driven by the vertically integrated pressure gradient at both sides of the Greenland-Scotland Ridge. It is controlled by differences in the density of the water masses as well as sea surface heights that are in turn related to the formation of dense, cold water masses, atmospheric circulation, and sea ice dynamics (Østerhus et al., 2001). The seasonal sea ice extent coincides with the Polar Front, which is the S-N boundary between the sea ice-covered Polar water and seasonally sea ice-free Arctic water. The Polar Front is at present situated northeast of Iceland; however, it shifts in concert with the Arctic front at (inter)annual as well as longer timescales (Hoff et al., 2016).

3. Material and Methods

3.1. Sediment Cores

The gravity cores P457-909 (62°50.20′N 12°59.47′W, 755-m wd, 758-cm core length, hereafter referred to as 909) and P457-905 (62°41.13′N 14°21.15′W, 1,610-m wd, 887-cm core length, hereafter referred to as 905) were retrieved from the southwestern flank of the IFR and south of the Icelandic shelf during the summer 2013 R/V POSEIDON Cruise P457 (Figure 1). The shallower core 909 was recovered from a thick levee covering the southwestern flank of the IFR, whereas the deeper core 905 was taken further down-slope (Werner & Nürnberg, 2014). Both cores display alternating intervals of (grayish) brown mud, and dark olive gray sandy mud to blackish gray volcanic muddy sands. The sediments are bioturbated to a minor extent with a few burrows up to 1 cm in diameter causing the occasionally mottled appearance of the sediments. Gravel (>4 mm)

and pebbles up to 8 cm are irregularly embedded in the fine-grained sediment matrix of both cores (Figure S1 in the supporting information). These clasts are derived as IRD and are dominantly composed of volcanic rocks with some rare occurrences of metamorphic, igneous rocks, and detrital carbonate. Complementary box cores reveal that only 7 and 10 cm of the topmost sediment including the sediment-water interface are unrecovered by the gravity cores 905 and 909, respectively. Since samples have been only taken from the gravity cores 905 and 909, core depths refer to the gravity sediment cores only.

3.2. Sample Preparation

The cores were split lengthwise into two halves; one half was subsampled into 1-cm-thick slices. The sediment samples were weighed before and after freeze drying to determine the water content. Approximately 4–5 g of the dried samples were processed for the grain size measurements. The rest of the bulk sediment sample was freeze dried and weighed prior to wet sieving at 63 μm using a fine water spray. The coarse fraction >63 μm was dried in an oven at 40 °C and weighed to determine the percentage of bulk fraction >63 μm containing detrital and biogenic components. The coarse fraction was subsequently split by dry sieving into three size fractions: 63–125, 125–250, and >250 μm. Different foraminifera species were then selected and processed for stable isotope measurement.

3.3. XRF Core Scanning

XRF core scanning provides rapid, nondestructive and high-resolution records of element contents of marine bulk sediments (Richter et al., 2006; Weltje & Tjallingii, 2008). XRF core scanning was carried out on the surfaces of the archive halve using an Avaatech XRF core scanner at the Department of Marine Climate Research, Institute of Geosciences, Kiel University (Germany). The sediment surface was carefully cleaned and covered with SPEXCerti Ultralene® foil to avoid contamination of the instrument sensor and desiccation of the sediment surfaces. The reproducibility was monitored by analyzing in-house XRF standards before and after each measuring session and compared to the long-term record. Qualitative XRF measurements expressed in counts per seconds were taken every 1 cm for 10 s, with a generator setting of 10 kV for the relatively light elements Fe, Al, Si, S, Cl, Ca, K, Mn, and Ti, whereas the heavier elements (Br, Rb, Sr, and Zr) were measured at 30 kV. Ratios of elemental intensities (e.g., Ti/K, Zr/Rb, Ca/Fe, and Ca/Sr) are expressed on a logarithmic scale, since they are linearly related to their concentrations and can be reversibly scaled (e.g.,Richter et al., 2006; Weltje & Tjallingii, 2008). The high-resolution records of the XRF ratios allowed for stratigraphic linkages between cores 905 and 909 as well as to the other cores in the region, and $\delta^{18}O$ record of Greenland NGRIP ice core (Figure 2).

3.4. Grain Size Analysis

The lithogenic fraction of samples was isolated prior to grain size analysis by removing the organic matter, carbonate and biogenic silica (e.g., diatom frustules) using H_2O_2 (30%), HCl (0.5%), and NaOH, respectively (cf. Jonkers et al., 2015). The lithogenic grain size volume distributions were measured using a Sympatec HELOS/KR laser diffraction particle-size analyzer at a wide size range (57 classes between 0.12 and 2,000 μm) at the Laboratory for Sediment Analysis, the Vrije Universiteit (Amsterdam, the Netherlands). Before analyzing, the samples were passed through a sieve with a mesh size of 2 mm. Overall, grain size distributions were determined on 299 samples (core 909; $n = 143$, core 905; $n = 156$), preselected on the basis of the XRF log (Zr/Rb) and log (Ti/K) records of both cores to cover the full range in lithogenic particle composition. Grain size samples were also taken from volcanic ash layers at 176.5 cm in core 909 and at 359.5 and 360.5 cm in core 905. Seventeen samples were randomly measured in duplicate (Figure 3c) to determine the reproducibility of the grain size measurements, which yield a mean coefficient of determination (r^2) better than 0.95 with a lower reproducibility for the less abundant grain size classes >354 μm.

3.5. Grain Size End-Member Modeling

End-member modeling of the grain size distributions allows for the decomposition into the statistically evident subpopulations, which are characteristic for different modes of sediment transport and deposition (Prins et al., 2002; Prins & Weltje, 1999). Accompanying grain size determination of the sand fraction is important to examine the possible IRD contribution to the overall grain size distributions (Hoffmann et al., 2019; McCave & Hall, 2006; Prins et al., 2002). The grain size data set was separated into statistically significant end-members using the Analysize program in Matlab (Paterson & Heslop, 2015). This approach has been shown to reliably determine grain size end-members (Van Hateren et al., 2018) and has been

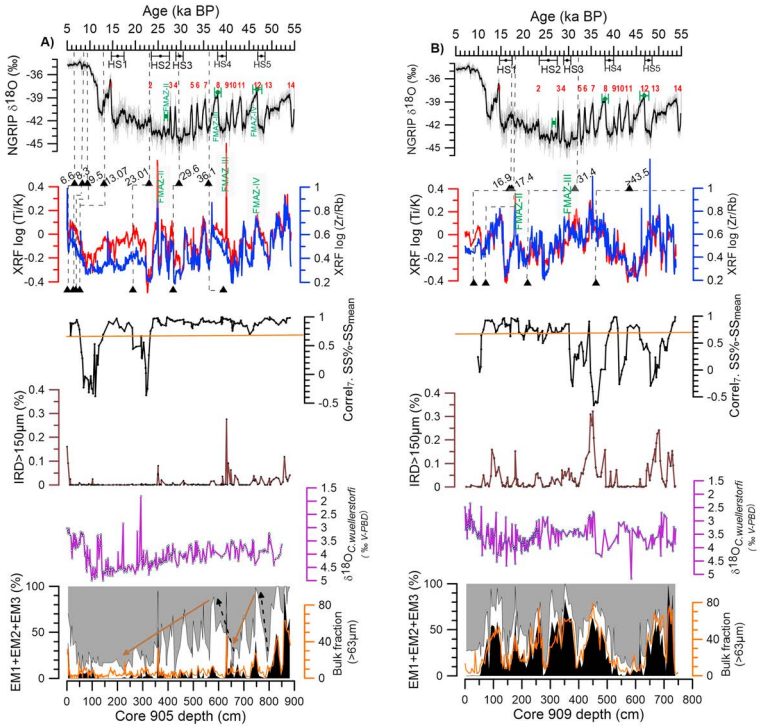

Figure 2. Proxy records of cores 905 (a) and 909 (b) versus core depth in relation to the NGRIP $\delta^{18}O$ record for reference (Svensson et al., 2008). For each core, the calibrated accelerator mass spectrometry (AMS) ^{14}C (radiocarbon) ages (black triangles) are plotted both at their respective core depths and related to the NGRIP $\delta^{18}O$ record. The positions of the FMAZ-II, FMAZ-III, and FMAZ-IV are given for both cores and marked within the NGRIP $\delta^{18}O$ record by green circles (including uncertainty in age). The plotted proxy records comprise XRF log (Ti/K) ratios, log (Zr/Rb) ratios, coefficients of a 7-point downcore correlation of sortable silt (10–63 μm) means and percentages with a horizontal line of $r = 0.7$ for references, lithogenic fraction >150 μm (i.e., IRD), EM abundances (EM1 + EM2 + EM3 = 100%; EM1 = black, EM2 = white, EM3 = gray), size fraction >63 μm (in orange), and $\delta^{18}O$ values of benthic foraminifera. Red numbers along the NGRIP $\delta^{18}O$ record mark Greenland Interstadials. Greenland stadials associated with major Heinrich events with upper and lower limits above the NGRIP $\delta^{18}O$ record are indicated by black horizontal bars (Rasmussen, Thomsen, et al., 2014). Dashed black arrows indicate increasing trend of EM2 toward GIs, most prominent toward the long-lasting GI-8 and GI-12. Brown arrows mark the decline of bottom current intensities from G-I8 to LGM and from GI-12 to G-I8. BP = before present; EM = end-member; FMAZ = Faroe Marine Ash Zone; HS = Heinrich Stadial; IRD = ice-rafted debris; NGRIP = North Greenland Ice Core Project; XRF = X-ray fluorescence.

applied to other marine sediment cores from the region to reconstruct changes in bottom current speed and IRD input (Hoffmann et al., 2019; Jonkers et al., 2009, 2015; Prins et al., 2002).

Most grain size samples have polymodal grain size distributions indicating the contribution of different grain size populations to the deposition sites. A three end-members solution explains more than 90% of observed variations in cores 905 and 909 (Figure 3a). The exclusion/inclusion of volcanic ash samples does not significantly affect the grain size distributions of the modeled end-members or their abundances. A four end-member solution does not improve the overall statistical fit between observed and modeled grain size distributions significantly (Figure 3b).

The finest-grain end-member (end-member 3, EM3) has its mode at ~8 μm within the fine-medium silt fraction (Figure 3d). The highest frequencies of end-member 2 (EM2) are centered on ~44 μm in the very coarse silt fraction. The coarse-grained end-member 1 (EM1) has a slight bimodal grain size distribution with a minor mode at ~8 μm (fine-medium silt fraction) and the dominant one at ~149 μm (fine sand fraction). For comparison, the percentage and the mean of sortable silt (SS) fraction (10–63 μm) were obtained using the approach of McCave and Andrews (2019) as indicator for flow speed sorting. In parallel, the grain size fraction >150 μm was calculated as an indicator for IRD, since this fraction is hardly transported by near-bottom currents. Additional grain size properties were calculated with the Excel application Gradistat using the Folk and Ward graphical method (Blott & Pye, 2001).

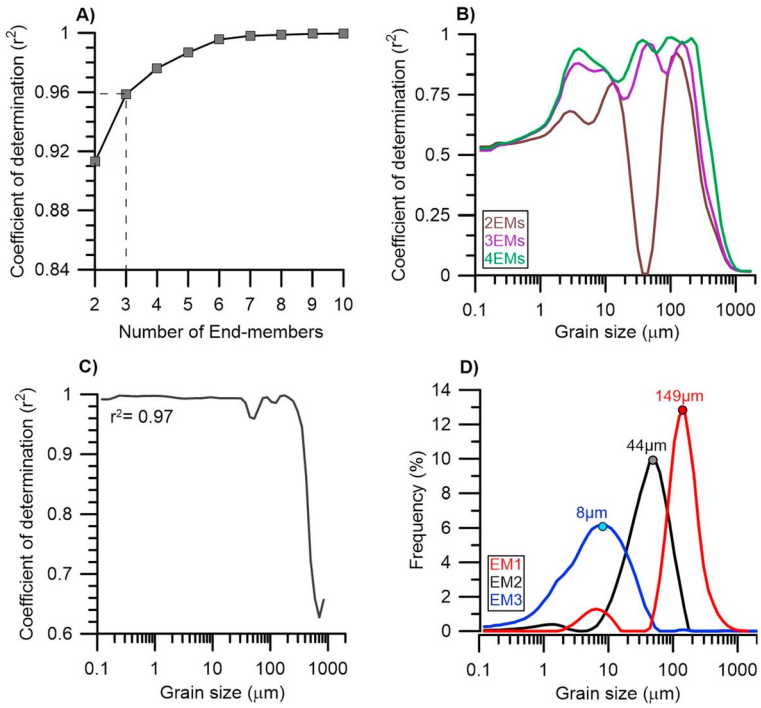

Figure 3. End-member (EM) modeling of grain size distributions for sediment cores 905 and 909. (a) Median coefficients of determinations between the observed and modeled grain size distributions are given for 2 to 10 EM solutions. The three EM solutions used in this study explain about 96% of the observed grain size variations. (b) Coefficients of determination for each grain size class (EMs) that were used to determine the optimal number of end-members. The three EM solution yields much higher coefficients of determination for each of the grain size classes compared to a two-EM solution, whereas a four-EM only slightly improves the statistical fit. (c) Replicate grain size measurements were randomly performed on 13 samples of core 905 and four samples of core 909, which provide a mean coefficient of determination (r^2) of ~0.97 (d) The grain size distributions of modeled EMs are shown, whereby the finest (EM3), medium (EM2), and coarse (EM1) EMs are plotted in blue, black, and red, respectively, together with their dominant modes.

3.6. Stable Isotope Analysis

Calcitic tests of the epifaunal foraminiferal species *Cibicidoides wuellerstorfi* were selected from the >250-μm size fraction for stable oxygen and carbon isotope analyses ($\delta^{18}O$ and $\delta^{13}C$). To examine the provenance of detrital carbonates, subsamples of seven individual detrital carbonate grains were measured in duplicate for their $\delta^{18}O$ and $\delta^{13}C$ values (Figure S2 and Table S3). The $\delta^{18}O$ and $\delta^{13}C$ measurements were performed on a Thermo Fisher Scientific MAT 253 mass spectrometer equipped with an automated CARBO Kiel IV carbonate preparation device at GEOMAR, Helmholtz Centre for Ocean Research Kiel, Ocean Circulation and Climate Dynamics (Germany). The $\delta^{18}O$ and $\delta^{13}C$ values were calibrated against the NBS-19 (National Bureau of Standards) standard and reported in per mil relative to the Vienna Peedee Belemnite scale. The long-term external reproducibility was monitored by an in-house Bremen Solnhofen Limestone standard with an analytical precision of ±0.03‰ for $\delta^{13}C$ and ±0.06‰ for $\delta^{18}O$.

3.7. Radiocarbon Dating

Twelve accelerator mass spectrometry radiocarbon (AMS ^{14}C) ages were determined from mixtures of planktonic foraminifera (*Globigerina bulloides* and *Neogloboquadrina pachyderma* [sinistral]; >250-μm size fraction) at Beta Analytic Inc., Miami, Florida (USA). The conventional radiocarbon ages have been corrected for the total isotopic fractionation effects and were calibrated following the mathematical approach of Talma and Vogel (1993) and the MARINE13 database (Reimer et al., 2013) using a global marine reservoir age of 400 years with a local reservoir correction of $\Delta R = 45 \pm 5$ years (http://calib.org/marine/). The calibrated AMS ^{14}C ages are reported as radiocarbon dates before present (BP; Table 1).

Table 1
Accelerator Mass Spectrometry ^{14}C Ages Measured on Mixtures of Planktonic Foraminifera Globigerina bulloides and Neogloboquadrina pachyderma (Sinistral)

Core	Mean depth (cm)	Sample ID (Beta Lab)	Conventional ^{14}C age (years BP)			Median calibrated ^{14}C age (2σ; years BP)		
P457-905	1.5	439866	6,270	±	30	6,673	±	33
P457-905	24.5	429027	7,960	±	30	8,388	±	33
P457-905	35.5	439867	8,900	±	40	9,502	±	50
P457-905	50.5	409855	11,630	±	40	13,076	±	64
P457-905	260.5	409856	19,570	±	70	23,013	±	80
P457-905	420.5	409857	25,980	±	120	29,612	±	132
P457-905	618.5	429028	32,670	±	230	36,138	±	198
P457-909	30.5	409858	14,430	±	50	16,991	±	84
P457-909	73.5	429029	14,770	±	50	17,488	±	68
P457-909	220.5	409859	28,190	±	150	31,445	±	100
P457-909	460.5	409860	>43,500					

4. Results

4.1. Chronostratigraphy of the Sediment Cores

4.1.1. AMS ^{14}C Ages

The uppermost sediments of gravity core 905 (1- to 2-cm core depth) yield a calibrated AMS ^{14}C age of 6,673 ± 30 years BP, whereas gravity core 909 provide an age of 16,991 ± 50 years BP at 30- to 31-cm core depth. A ^{14}C dead sample (extremely low ^{14}C activity, Beta lab's internal AMS limits) indicates that core 909 sediments below 460.5-cm core depth are definitely older than 43.5 ka BP. In core 905, AMS ^{14}C dates range from 6,673 to 36,138 years BP. The AMS ^{14}C dates (Table 1) reveal coherent age-depth relationships for both cores 905 and 909 (Figures 2 and 4). Regional ^{14}C surface reservoir ages could deviate considerably from the global marine reservoir age with a maximum of ~1,500–2,000 years during Heinrich Events (Olsen et al., 2014; Voelker et al., 2000). The relatively low number of ^{14}C ages in combination with a few distinct regional tephra layers with a known age does not allow us to decipher the effect of local marine reservoir ages on our core chronologies, which is also beyond the scope of this study.

4.1.2. Tephrostratigraphy

Complementary to AMS ^{14}C ages, the tephrostratigraphy provides direct linkages between regional marine records and Greenland ice cores (Abbott & Davies, 2012; Davies et al., 2010). In cores 905 and 909, volcanic ashes that appear as distinct, patchy, and bioturbated intervals can be linked to regionally widespread ash falls from Icelandic and Faroe Island volcanoes, which is confirmed by comparative geochemical analyzes

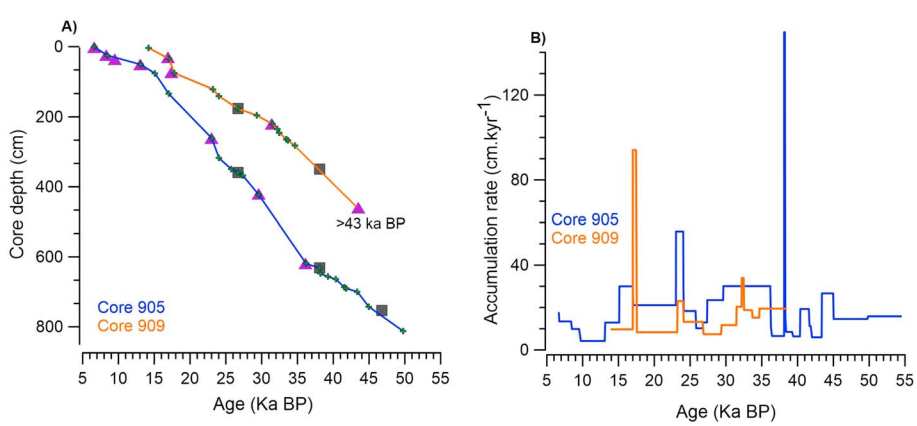

Figure 4. (a) Age-depth relationships of sediment cores 905 (1,610-m water depth, blue line) and 909 (755-m water depth, orange line). The chronostratigraphy is based on calibrated accelerator mass spectrometry ^{14}C ages (purple triangles) and identified tephra layers (black squares), and the tuning of prominent X-ray fluorescence elemental peaks to Northern Hemisphere Greenland Interstadials and Greenland Stadials (green crosses; Figure 2 and Tables 1 and 2). (b) Accumulation rate of cores 905 (blue) and 909 (orange) for the last ~55-6 ka before present (BP).

Table 2
Depth Ranges of Geochemically Identified Volcanic Ash Layers in Cores P457-905 and 909 as Reported by Bonanati et al. (2016)

Gravity core	Core depth (cm)	Composition	Appearance	Reported age	Greenland Interstadial (GI)
P457-909	176.5* (173.5–178.5)	Tephra F/ FMAZ II,	Distinct tephra layer	26,740 ± 390 years (b2k)[a]	After GI-3
P457-905	359.5* (357–361)	Kverkfjöll volcanic system	Distinct tephra layer		
P457-905	631.5* (629.5–633)	Grímsvötn /FMAZ III	Distinct tephra layer	38,122 ± 723 years (b2k)[a]	~100 years after the
P457-909	~350		Shards		onset of GI-8
P457-905	753.75 (753.5–754.5)	FMAZ IV	Diffused tephra zone	46,800 ± 1,000 years[b]	Early phase of GI-12

Note. The ashes were used to link both sediment cores stratigraphically and to provide additional age-depth markers. The midpoints of the distinct volcanic ash layers that are derived from maxima in XRF log (Ti/K) and log (Zr/Rb) by this study are indicated by asterisks.
[a]Svensson et al. (2008). [b]Wastegård and Rasmussen (2001); Griggs et al. (2014).

(Bonanati et al., 2016; Table 2). Thick volcanic ash layers of the Faroe Marine Ash Zone (FMAZ)-II and FMAZ-III centered on 176.5 and 631.5 cm are well preserved with sharp upper and lower contacts in core 905, whereas FMAZ-IV is only diffused in this core around 753.5 cm. In core 909, only FMAZ-II and FMAZ-III are present, implying that the older tephra FMAZ-IV was either reworked, eroded, or never deposited at this site (Figure 2).

Given the close proximity of these sites to Icelandic and Faroe Island volcanoes, these tephra layers were probably deposited as primary ash fall, therefore allowing direct linkages to NGRIP ice cores (Olsen et al., 2014). In Greenland ice cores, the FMAZ-II tephra is positioned ~1,000 years after the onset of GI-3, whereas FMAZ-III occurs ~100 years after the onset of GI-8 (Olsen et al., 2014). FMAZ-IV is deposited during early stage of GI-12 following HS-5 (Griggs et al., 2014; Wastegård & Rasmussen, 2001). Combining AMS ^{14}C ages of both cores with the identification of prominent volcanic ashes of known age (Tables 1 and 2 and Figures 2 and 4) provides a strong independent age control. For core 909, independent age constraints are unavailable to verify HSs older than FMAZ-III. Additional age constraints were derived by tuning of the comparable log (Ti/K) and log (Zr/Rb) records of core 905 and 909 to that of nearby cores ENAM93-21 and JM-FI-19PC from northeast of the IFR (Ezat et al., 2014; Richter et al., 2006).

4.1.3. Benthic Isotopes

The $\delta^{18}O_{C.\ wuellerstorfi}$ records document the transitions from Marine Isotope Stage (MIS)-3, MIS-2, and MIS-1. In core 905, the last deglacial termination is characterized by a sharp decrease in $\delta^{18}O_{C.\ wuellerstorfi}$ values (~2‰) toward interglacial. Several $\delta^{18}O_{C.\ wuellerstorfi}$ minima of <3.5‰ occur during 25–15 ka BP in both cores. Core 909 yields generally lower δ^{18}O values compared to the deeper core, some of which are accompanied by low δ^{13}C values (<0.8‰). The δ^{13}C records of core 905 and 909 show a comparable decrease from 1.6‰ to 0.6‰ during MIS-2, whereas 905 exhibits relative lower δ^{13}C values compared to 909 before MIS-2 (Figures 2 and 5).

4.2. Lithogenic XRF Records

The lithogenic XRF log (Ti/K) records of both cores generally vary between −0.4 and 0.4 at centennial to millennial timescale (Figures 2 and 5). The log (Ti/K) records resemble those of the nearby sediment cores ENAM93-21 and JM-FI-19PC to the northeast of the IFR (Ezat et al., 2014; Richter et al., 2006), for which detailed chronologies have been established by numerous AMS ^{14}C dates, tephra layers, and linkages of paleoceanographic proxy records to the δ^{18}O NGRIP record (Ezat et al., 2014; Hoff et al., 2016). Overall, elevated log (Ti/K) values correlate to GIs, whereas low values correspond to GSs and HSs. Minima in log (Ti/K) at ~140–168 cm and at ~323–359 cm in respectively 905 and 909 can be assigned to HS-2, whereas the younger minima coincide with HS-1. Subsequently, older minima in core 905 can be related to HS-3, HS-4, and HS-5. Core 905 displays an increase in log (Ti/K) during the last deglacial period (Figures 2 and 5). In the North Atlantic oceanic sector, spatiotemporal variations in (log) Ti/K are linked to changes in the proportion of the lithogenic sediment fraction originating from volcanic (Ti-rich) and felsic/acidic (K-rich) sediment source areas, respectively (Ballini et al., 2006; Gruetzner & Higgins, 2010; Jonkers, 2010; Richter et al., 2006).

Variations in log (Ti/K) display comparable patterns as the accompanying log (Zr/Rb) records in core 905 and 909. Zr is usually an indicator for the lithogenic sand fraction, since Zr is mostly present in silt-sized zircons, which usually sort together with the sand-sized siliciclastic fraction due to their high density (Lamy

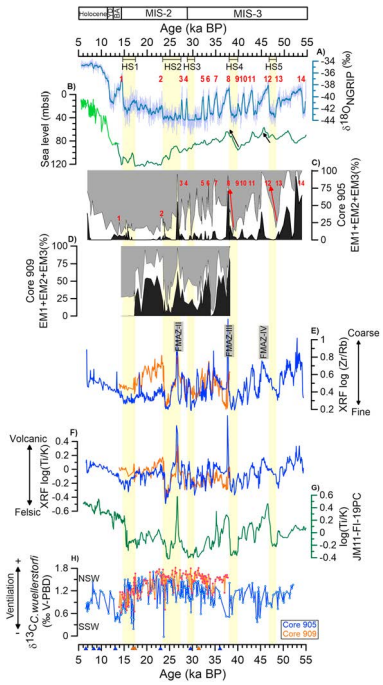

Figure 5. Iceland-Faroe Ridge overflow dynamics from ~55 to 6 ka BP inferred from paleoceanographic proxy records 905 (blue) and 909 (orange). (a) NGRIP $\delta^{18}O$ record including Greenland Stadials comprising HS-1 to HS-5 (yellow bars; Rasmussen, Bigler, et al., 2014). (b) High-resolution sea level reconstruction from Arz et al. (2007), dark green line) and Grant et al. (2014), light green line). Arrows show relative sea level rises during GIs. (c, d) Cumulative percentages of grain size EM1, EM2, and EM3 (EM1 + EM2 + EM3 = 100%; EM1 = black, EM2 = white, and EM3 = gray). GIs are denoted by red numbers. Significant weakening of bottom currents occurred during HSs as reflected in higher percentages of the fine-grained EM3. Progressive increases in EM2 percentages toward GIs reflect the strength of bottom currents. The arrows mark the gradual transition and increase of EM2 from GSs to GIs, which is most obvious for the relatively long-lasting D-O 8 and 12. (e) XRF log (Zr/Rb) ratios of cores 905 and 909. Core 909 is relatively coarser than core 905, particularly during Last Glacial Maximum. HSs are dominated by fine-grained sediments. FMAZ tephra layers are characterized by relatively coarse-grained particles. (f) XRF log (Ti/K) ratios of cores 905 and 909. Highest log (Ti/K) occur within the FMAZ layers and the lowest ratio is recorded during HSs. (g) In order to compare our XRF data with nearby core FM11-FI-19PC (northeast of the Faroe Islands) the XRF (Ti/K) ratios of this core are converted to a logarithmic scale and plotted against the age model of Ezat et al. (2017) and Hoff et al. (2016), which is based on AMS ^{14}C dates, tephra stratigraphy, and linkages of proxy records to NGRIP. The log (Ti/K) record of FM11-FI-19PC resembles those of core 905 and 909, although the onset of D-O 8 and D-O 12 is abrupt in 905, followed by gradual decreases toward GIs. (h) $\delta^{13}C$ records of the benthic foraminiferal species *C. wuellerstorfi*, whereby higher $\delta^{13}C$ values point to better-ventilated conditions possibly due to the overflow of well-ventilated NSW and from the Nordic Seas. Depleted benthic $\delta^{13}C$ values suggest less ventilation and/or intrusion of SSW. BP = before present; EM = end-member; FMAZ = Faroe Marine Ash Zone; GI = Greenland Interstadial; HS = Heinrich Stadial; MIS = Marine Isotope Stage; NGRIP = North Greenland Ice Core Project; NSW = Norwegian Sea Water; SSW = Southern Source Water; VPBD = Vienna Peedee Belemnite; XRF = X-ray fluorescence.

et al., 2015), whereas Rb often replaces K in clay minerals from felsic sources (Schneider et al., 1997). Relatively high log (Zr/Rb) values that are recorded between HS-2 and HS-1 in shallow core 909 marks coarse-grained sediment deposition compared to 905. On the other hand, maxima in log (Ti/K; >0.4) and log (Zr/Rb; >0.7) correspond to the distinct tephra layers of FMAZ-II (905 and 909) and FMAZ-III (905).

4.3. Lithogenic End-Member Abundances

The accumulation rates of the three end-members were estimated assuming linear accumulation rates for both cores for the timespan between 38 and 13 ka BP (Figure 6). Considerably lower accumulation rates of the finest end-member EM3 occurred at the shallow core site 909 than at the deep site 905, while the cumulative accumulation rates of EM1 and EM2 are proportional at both sites.

4.3.1. Coarse-Grained Sediment (EM1)

In core 905, the abundances of the coarsest end-member EM1 are generally low (<10%) except at the core top, the bottom part, and within the FMAZ-II and FMAZ-III layers. Maxima in EM1 are tentatively linked to GI-13 and GI-14 in core 905, whereas the abundances of EM1 show slight variability during MIS-3 with maxima up to 15%, generally lagging maxima of the intermediate end-member EM2. During the Last Glacial Maximum (LGM), EM1 is virtually absent in the lithogenic record, while 3% EM1 on average is present during HS-1 as well as in the core top of 905 (Figure 5). In core 909, EM1 is dominant with high abundances between HS-1 and HS-2, which are both characterized by low amounts of EM1 (<15%). The distinct FMAZ-II layers yield EM1 abundances over 50%.

For both cores, variations in the abundance of the coarse-grained end-member (EM1) agree remarkably well with the percentages of the bulk fraction >63 μm (Figures 2 and 6), which is attributed to the low $CaCO_3$ content of marine sediments, typically <10% in this region (Ballini et al., 2006). Slight deviations between percentages of the lithogenic EM1 and bulk fraction >63 μm might be partly due to the occurrence of detrital carbonates. Detrital fragments of carbonate rock (<1 cm) that occasionally occur in both cores yield average $\delta^{18}O$ values of −1.51‰ (±0.06; 1 *SD*) and $\delta^{13}C$ values of 2.03‰ (±0.03; 1 *SD*) for core 905 ($n = 14$, two measurements for each sample), which are within the isotopic ranges of carbonate bedrock from South England, Denmark, and North Sea (Scholle et al., 1974, 1983; Figure S2 and Table S3). Like Ca, Sr is mainly present in marine carbonates; therefore, high log (Ca/Sr) ratios are indicative of fine-grained detrital carbonates, which are derived as IRD from British and Fennoscandian ice sheets (cf. Hodell et al., 2010, 2008). High XRF log (Ca/Sr) ratio >1.1 occur at about 8.3, 13.3, 18.3, and 28.6 ka BP and at the base of core 905. It has to be noted, in this respect, that small and sparsely distributed detrital carbonates may have not been detected by XRF scanning.

4.3.2. Fine-Grained Sediment (EM2 and EM3)

In core 905, most of the end-member variations are due to changes in the admixture of EM2 and EM3, showing a clear sawtooth pattern reflecting D-O oscillations (Figures 2 and 5). The end-members reveal gradual coarsening from GSs to GIs, which is sharply terminated by fine-grained deposition during HSs. The sawtooth pattern is most obvious for D-O events 12 and 8 in core 905. The onset of D-O event 8 is constrained by the presence of FMAZ-III, which occurs ~100 years after the onset of

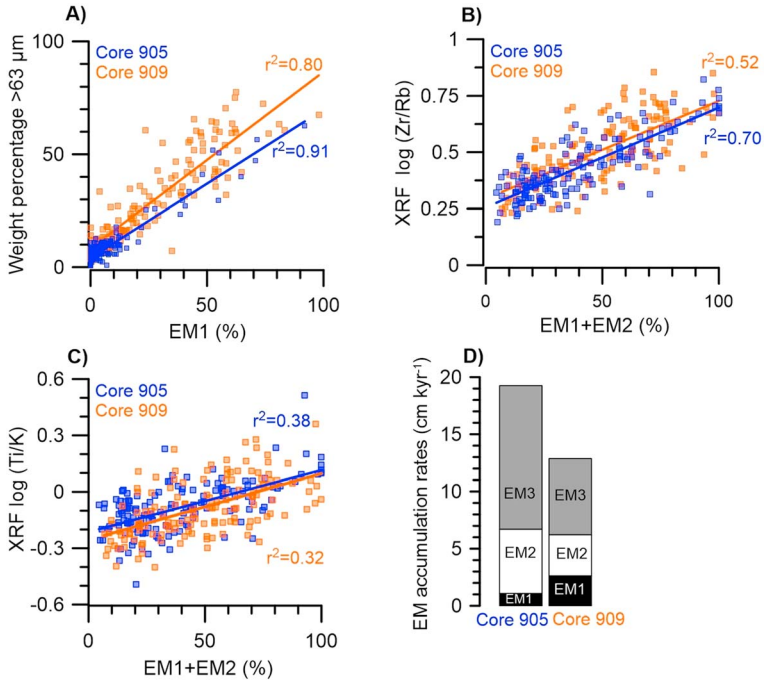

Figure 6. Correlations between (a) EM1 and the coarse bulk fraction >63 µm, (b) cumulative EM1 + EM2 percentages plotted against XRF log (Zr/Rb) ratios and (c) XRF log (Ti/K) ratio. Orange squares mark core 909; blue ones denote core 905. (d) Comparison of EMs fluxes of core 905 and 909 for the time period from 38 to 13 ka BP, where they overlap. The coarseness of lithogenic fraction in core 909 is reflected by the relatively high abundances of EM1. In core 909, the overall lower accumulation rate is mainly due to low accumulation rates of EM3 relative to EM1 and EM2, because of winnowing at high bottom current speeds. EM = end-member; XRF = X-ray fluorescence.

GI-8 in NGRIP ice core (Olsen et al., 2014). The maxima in EM2 decline from DO-12 to DO-9 and from DO-8 to LGM. In core 905, EM2 increases during the deglacial period, whereas high abundances of EM3 occur during HS-2, LGM, and HS-1 (Figures 2 and 5).

In core 909, most of the end-member variation is between EM3 and EM1, whereas D-O events are not obvious in the end-member record partially due to the low stratigraphic resolution. The interval between HS-1 and HS-2 is characterized by much higher abundances of EM1 than in core 905 that match the high log (Zr/Rb) values (Figures 2 and 5).

5. Discussion

5.1. IRD Contribution to the Southwestern Flank of IFR

The occasional occurrence of volcanic fragments (>0.3 cm; visual observation) reflects local IRD input from the Iceland and Faroe Islands, which were covered by extensive ice sheets during the last glacial period. These ice sheets extended onto the continental shelf edges with grounding lines at ~200 m below the present-day sea surface (Boulton et al., 1988; Hubbard et al., 2006). Additional IRD can be derived from sea ice with basal freeze-on of coarse-grained shelf sediments (Andrews, 2000; Nürnberg et al., 2011). Some rare IRD of other rock types originate from icebergs, which is presumably calved from more distal ice sheets. Taking into account the prevailing northbound surface currents as part of the glacial anticlockwise North Atlantic gyre (Maslin, 1995; Peck et al., 2006; Seidov & Prien, 1996), the British and Fennoscandian ice sheets would have been the most likely source area for detrital carbonates. Widespread IRD layers were deposited in the North Atlantic, especially within the so-called Heinrich Belt (Bond et al., 1992; Heinrich, 1988) and offshore the British Ireland Ice Sheet (BIIS; Scourse et al., 2009) during HSs, as a result of massive iceberg and meltwater discharge due to instabilities of the Laurentide and European ice sheets.

Due to the considerable amounts of fine-medium sands present in icebergs (Jonkers et al., 2015) the lithogenic fraction >150 µm is considered a qualitative indicator for IRD in deep-sea sediments rather than

rarer gravel and pebbles (e.g.,Rasmussen et al., 1998). Ice rafting events would therefore increase the abundance of coarse-grained EM1 in cores 905 and 909. However, the EM1 records from the southwestern flank of the IFR do not reveal systematic IRD increases during HSs. The lack of IRD in cores 905 and 909 can be explained by their geographic position, outside the main path of iceberg discharge in the North Atlantic during HSs (Bond et al., 1992; Heinrich, 1988). Moreover, the contemporaneous massive iceberg release in the Nordic Seas did not generate widespread IRD deposits during HSs, since the icebergs were relatively sediment barren (Dowdeswell et al., 1999). Moreover, the shallow depth of the nearby IFR during glacial sea-level low stands could have hampered the passage of icebergs as is indicated by extensive plough marks at the IFR (Dorn & Werner, 1993; Masson et al., 2004; Puteanus & Werner, 1990). Finally, an extended sea ice cover around the IFR would have slowed down melting of icebergs (Hoff et al., 2016). The absence of coarse-grained IRD in our cores agrees with the grain size minima in core ODP 984, retrieved from the Reykjanes Ridge near the southwest coast of Iceland (Praetorius et al., 2008). Since the influence of IRD on the grain size distribution seems to be inconsequential for these coring sites, other transport mechanisms would have exerted a major control on the EM1 deposition.

5.2. Aeolian Sediment Input

Given the proximity to Iceland, coring sites 905 and 909 might have received coarse-grained volcanic particles (50–100 μm), which have been reported to travel more than 2,000 km during severe storms (Navrátil et al., 2013). Today, aeolian dust deposition rates of 50 to 500 $g \cdot m^{-2} \cdot year^{-1}$ have been inferred for offshore areas near the southern coast of Iceland, which decline to much lower rates of 2–5 $g \cdot m^{-2} \cdot year^{-1}$ close to our coring sites (Arnalds et al., 2014, 2016). This is volumetrically small compared to the past accumulation rates at these core sites (Figure 4). Today, aeolian input southeast offshore Iceland is high due to the exposure of large sand plains by the current glacier retreat and prevailing southerly winds compared to the last glacial period, when large parts of Iceland and Faroe Islands were covered by ice sheets (Hubbard et al., 2006; Nørgaard-Pedersen et al., 2003). However, under rising eustatic sea levels and/or increasing current strength, glacial, aeolian, and riverine deposits could have been redistributed by near-bottom currents to greater water depths.

5.3. Near-Bottom Current Transport

Unlike most other deep-sea coring sites, where bottom currents are rarely capable of transporting considerable amounts of clastic sands (McCave & Hall, 2006), the IFR sites are situated at relatively shallow water depths and close to the present-day main flow axis of ISOW as indicated by the modern large-scale sandy contourite bedforms (Dorn & Werner, 1993). With increasing particle size, sediments become less prone to reworking and are therefore deposited close to their source areas. It has been postulated that the coarse-grained sediments of present-day contourite bedforms have been derived from upstream source areas rich in IRD (Dorn & Werner, 1993). In turn, high abundances of EM1 can therefore be indicative of past maxima in bottom current speeds, whereby finer-grained material is transported and deposited progressively downstream at lower current speeds. Small portions of EM3 that are present in intervals dominated by EM1 are probably deposited as interstitial mud in between the coarse sediment particles (McCave & Hall, 2006). The slightly higher accumulation rate of EM1 at core site 909 (Figure 6) can most likely be explained by the proximity to coarse-grained sediment sources and elevated bottom current speeds at the shallower water depths.

The intermediate EM2 has its mode in the noncohesive very coarse silt fraction (44 μm), which is usually subject to selective sediment transport and deposition by bottom currents (cf. SSs; McCave & Hall, 2006). In contrast, EM3 is dominated by the cohesive sediment fraction (<10 μm) that settled from suspension as aggregates at the seafloor. At turbulent flow, these aggregates fall apart and are transported further downstream (McCave & Hall, 2006). As a consequence, the accumulation of fines is suppressed under relatively strong bottom current conditions (Manighetti & McCave, 1995; McCave & Hall, 2006). Relatively high portions of EM3 therefore mark calm depositional conditions and weaker bottom currents having a lower ability to transport the coarser grained fraction (i.e., EM2). Significant correlations between means and percentage of SSs (10–63 μm) indicate that the majority of the silt fraction was current sorted for both cores (cf. McCave & Andrews, 2019) and were not readily affected by input of IRD (Figure 7). Interestingly, some intervals that show weak correlations between both silt parameters coincide with HSs, which is most obvious for core 905 (Figures 2 and 7). This suggests that during HSs, the near-bottom currents were too

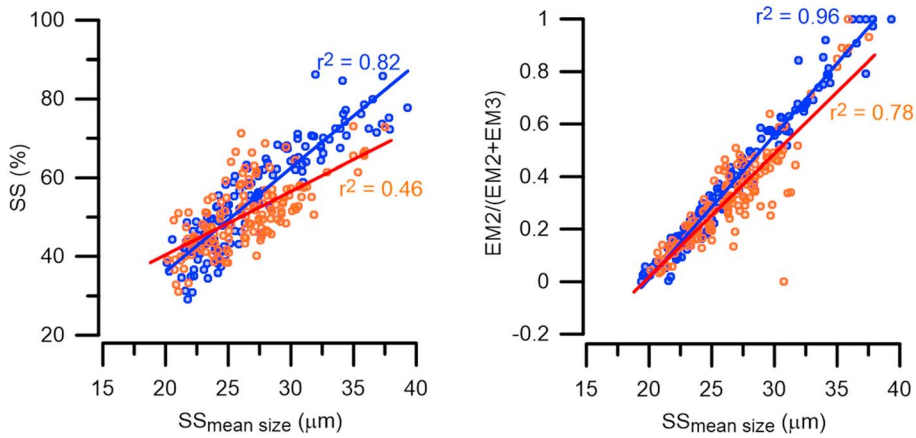

Figure 7. (a) Cross plot of the mean sortable silt (SS) fraction (10–63 μm) and the percentage of silt within the fraction ≤63 μm of core 905 (blue circles) and core 909 (orange circles). (b) Cross plot of the SS mean and the ratio between EM2/(EM2 + EM3). EM = end-member.

weak to redistribute the silt fraction, which is possible mainly deposited as fine-grained IRD. The significant relationship between the SS mean and EM2/(EM2 + EM3) indicates that the end-member ratios also document current-induced changes in sorting.

The overall lower accumulation rate at shallow core site 909 is mainly due to the low accumulation rates of EM3 relative to EM1 and EM2 (Figure 6). The low accumulation rate of EM3 can in turn be attributed to an enhanced winnowing of the finest fractions by bottom currents at shallower water depth. Increasing accumulation rates of the cohesive fraction (i.e., EM3) with greater depth were also found in a transect of sediment cores south of Rockall Trough/Gardar Drift (Manighetti & McCave, 1995).

The variations between the finest (EM3) and coarse-grained end-members (EM2 + EM1) are strongly correlated with the log (Zr/Rb) records and to a lesser extent with log (Ti/K), whereby EM3 shows affinity with K and Rb (Figure 6). The decoupling of temporal variations in grain size and log (Ti/K) indicate that grain size record is rather affected by changes in near-bottom speed than in provenance changes through time.

5.4. Bottom Current Dynamics Southwest of IFR

5.4.1. Greenland (Heinrich) Stadials

In cores 905 and 909, HSs are evident as pronounced intervals of felsic-rich fine-grained sediments (dominantly EM3; Figure 5) similar to sediment cores from NE of the Faroe shelf (e.g., Ballini et al., 2006). It has been postulated that the deposition of the fine-grained felsic sediments north of the IFR was facilitated by a weak current system, which was reversed in flow direction compared to present day (Rasmussen et al., 1998; Rasmussen & Thomsen, 2004). At the onset of HSs, the open ocean convection shifted from the Nordic Seas to the North Atlantic, together with the Polar Front and locus of NADW formation, due to the massive discharge of meltwater at both sides of the IFR (Barker et al., 2015; Maslin, 1995; Rasmussen, Thomsen, Labeyrie, & van Weering, 1996). The occurrence of "warm" Atlantic benthic foraminifera species and high (>3.5 °C) bottom water temperatures north of the IFR (Figure 8) are consistent with the northward intrusion of warm North Atlantic Intermediate Water through the FSC underneath a layer of cold, low-salinity surface water (Ezat et al., 2014; Rasmussen et al., 2016; Rasmussen & Thomsen, 2004). Consequently, the Hebrides and West Shetland shelves that received high input from mouth fans fed by one of the largest ice streams from the BIIS (i.e., Minche Ice Stream; Scourse et al., 2009; Figure 1) are then the most likely sources for the fine-grained felsic sediments. The lowest log (Ti/K) values of <−0.5 reflecting the highest contribution of felsic sediments on both sides of the IFR are indeed comparable to those values observed in surface sediments of the Rockall Trough (Figure 5) near the Barra Fan Ice Stream (Jonkers et al., 2012). If a northward-flowing bottom current along the BIIS margin derives the felsic material observed at all core sites, then it must have diverted into one branch continuing its way through the FSC and another splitting from the FBC outlet and continuing along the southwestern flank of the IFR around our core site (Figure 1). The latter is in agreement with the persistence of an anticlockwise circulation during glacial periods (Sarnthein et al., 1995).

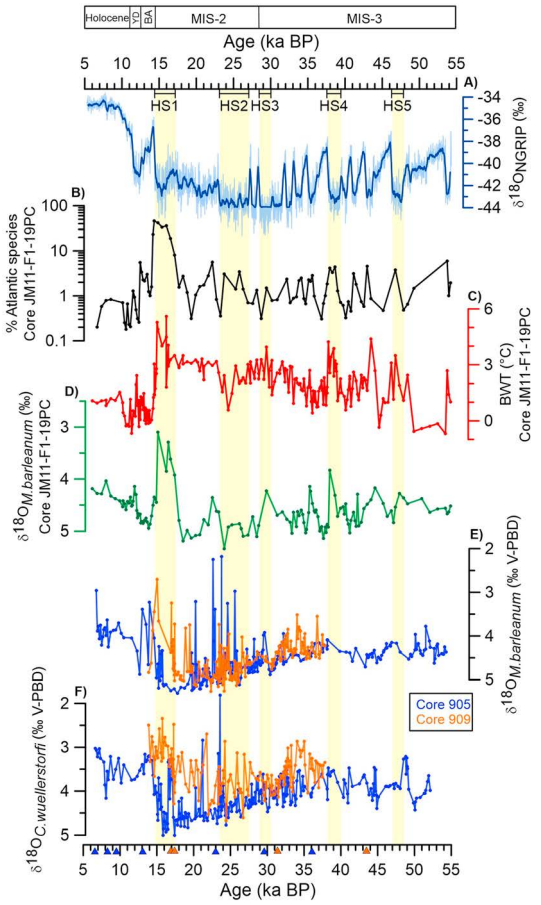

Figure 8. (a) NGRIP $\delta^{18}O$ record showing Greenland Stadials (yellow bars), which partly comprise Heinrich events. (b, c) The benthic faunal assemblage variations and reconstructed BWT in core JM11-F1-19PC (Ezat et al., 2014) imply that HSs are dominated by Atlantic species indicative of relatively warm intermediate water (Rasmussen, Bigler, et al., 2014). (d) $\delta^{18}O$ records of the benthic foraminifera species *M. barleanum* in core JM11-F1-19PC (Ezat et al., 2014). (e) *M. barleanum* $\delta^{18}O$ records of cores 905 (blue) and 909 (orange) following each other particularly during 15–35 kyr. (f) $\delta^{18}O$ values of the benthic foraminifera species *C. wuellerstorfi* in cores 905 (blue) and 909 (orange). Partly, the low $\delta^{18}O$ values (particularly during HS-1) in core 909 were most likely caused by intermediate water warming as recorded in this region (Ezat et al., 2014). Greenland Stadials associated with major Heinrich events are indicated by yellow bars (Rasmussen, Thomsen, et al., 2014). BWT = bottom water temperatures; FMAZ = Faroe Marine Ash Zone; HS = Heinrich Stadial; MIS = Marine Isotope Stage; NGRIP = North Greenland Ice Core Project; V-PDB = Vienna Peedee Belemnite.

Depleted benthic $\delta^{18}O$ values near the IFR suggest the persistence of convection during HSs, probably by local brine injection due to sea ice formation (Vidal et al., 1998). Additionally, the $\delta^{13}C$ values of benthic foraminifera indicate that core sites 905 and 909 were generally bathed in well-ventilated waters (Figure 8). These observations leave the possibility that the local convection of low-salinity, cold surface waters maintained a weak overflow across the Iceland-Scotland Ridge during HSs, which also selectively transported fine-grained felsic sediments from northern felsic sources. A potential source area is the nearby North Sea Fan that is fed by the Norwegian Channel Ice Stream, one of the major drainages of the Scandinavian Ice Sheet (Hughes et al., 2016; Patton et al., 2017; Scourse et al., 2009). Under such a scenario, the observed warming of the deeper water masses north of the IFR can be explained by heat trapping under the low-salinity and cold surface waters during Heinrich events (Dokken et al., 2013). However, this scenario also invokes a limited transport of volcanic sediments from the IFR, which can be attributed to the coarseness of Ti-rich volcanic sediments relative to the weak bottom current strength and/or a restricted flow across the crest of IFR.

5.4.2. GIs

Due to warming and the northward shift of the Polar Front at the onset of GIs, the open ocean convection and the locus of deep-water formation most likely shifted north of the IFR, which led to a strong southward overflow across the IFR comparable to today (Keigwin et al., 1991; Rasmussen et al., 2016). The increasing strength of the near-bottom currents enhanced the transport of relatively coarse-grained Ti-rich sediments from the IFR volcanic source area (Figures 5 and 6). The progressively rising eustatic sea level (Arz et al., 2007; Grant et al., 2014) further increased the bottom current-driven sediment transport across the IFR in addition to flow through the Faroe Channels (FSC and FBC; Figure 5).

The sedimentary records ENAM93-21 and JM11-FI-19PC retrieved north of the FSC (Figure 1) reveal abrupt increases in volcanic sediment deposition followed by gradual decreases toward the HS (Ezat et al., 2017; Hoff et al., 2016; Richter et al., 2006). This change in sedimentary provenance is coeval with the temperature evolution documented in Greenland ice cores. In contrast, cores 905 and 909 from the southwestern flank of the IFR recorded the opposite pattern: a gradual increase in volcanic sediments during GIs declined by the felsic fine-grained sediment deposition during HSs (Figures 2 and 5). This discrepancy most likely reflects the cumulative effect of (1) near-bottom currents through the Faroe Channels and (2) overflow cascading over the IFR at the core sites 905 and 909, while ENAM93-21 and JM11-FI-19PC cores are exclusively affected by water masses entering the Faroe Channels.

As the bottom current signal recorded in ENAM93-21 and JM11-FI-19PC appears to be a more direct response of warming and subsequent increasing convection, sites 905 and 909 experienced both an increased overflow across the ridge crest under the eustatic sea level rise and through the Faroe Channels. As a consequence, GIs sea level rise allowed widening the IFR gateway and the transport of relatively coarse-grained volcanic sediments. The progressively rising sea level likely promoted dense Nordic Sea waters to cross the IFR amplifying the D-O oscillations as recorded in log (Ti/K) records of core 905. The enhanced downstream sediment transport from IFR volcanic sources during GIs led to high log (Ti/K) ratios, MS, and smectite content at downstream core sites in the Icelandic Basin (Ballini et al., 2006; Kissel, 2005; Kissel et al., 1999). Additionally, the vertical shift of the main flow

Table 3
Geographical Positions and Water Depth of Studied and Nearby Sediment Cores

Core	Lat.	Long.	wd (m)	Location	References
P457-909	62°50.20′N	12°59.4′W	755	SW flank of IFR	This study
ENAM93-21	62°44.00′N	3°52.92′W	1,020	NE of Faroe Islands	Rasmussen, Thomsen, Weering, & Labeyrie, (1996)
JM11-F1-19PC	62°49′N	3°52′W	1,179	NE of Faroe Islands	Ezat et al., (2014); Hoff et al., (2016)
LO09-18	58°58.04′N	30°40.99′W	1,471	Reykjanes Ridge	Prins et al., (2001); Jonkers, (2010)
S08-05GGC	59°11.17′N	30°54.29′W	1,420	Western flank of Reykjanes Ridge	Snowball & Moros, (2003)
S08-07GGC	59°00.70′N	30°36.11′N	1,580	Reykjanes Ridge	Snowball & Moros, (2003)
MD99-2247	59°04.61′N	31°28.34′W	1,690	Reykjanes Ridge	Ballini et al., (2006)
P457-905	62°41.13′N	14°21.15′W	1,610	SW flank of IFR	This study
DS97-2P	58°56.33′N	30°24.59′W	1,685	Eastern flank of Reykjanes Ridge	Prins et al., (2001)
IODP U1314	56°21.9′N	27°53.3′W	2,820	Eastern flank of Reykjanes Ridge	Grützner & Higgins, (2010)
KN166-14-13JPC	53°3.41′N	33°31.7′W	308	Eastern flank of Reykjanes Ridge	Hodell et al., (2008)
IODP U1308	49°52.66′N	24°14.28′W	3,871	Southern Gardra Drift	Hodell et al., (2008)

axis is likely responsible for the inferred increase in bottom current speed at core site 905 during GI sea level high stands (Figure 5). However, a comparable sawtooth pattern as in core 905 with gradual intensification of bottom currents followed by a sharp decline has also been recorded at core sites along the western and eastern flank of Reykjanes Ridge (SO82-07GGC, 1,580-m wd; LO09-18GC, 1,460-m wd; SO82-05GGC, 1,420-m wd; MD99-2247, 1,690-m wd; Figure 1 and Table 3). This suggests that the bottom current circulation along the Reykjanes Ridge is strongly controlled by overflow cascading over the IFR.

5.4.3. LGM

During the LGM, sea level was lower by at least ~120 m (Arz et al., 2007; Waelbroeck et al., 2002) and glaciers propagated onto Iceland and the Faroe shelves, both shallowing and narrowing the IFR gateway. Ice sheets extended off the Iceland shore with grounding lines ~200 m below present sea level during the LGM (Boulton et al., 1988; Ingólfsson et al., 1997). The proximity of the ice shelf grounding line probably contributed the relatively high EM1 flux at the shallow core site 909 (Figures 2 and 5). On the other hand, the sediment coarseness (high EM1 and log [Zr/Rb]) can be linked to relatively strong bottom currents at shallow site 909 during the LGM (Figures 2 and 5), which is in agreement with a shoaled ISOW and shallower mode of circulation as recorded in other sediment cores from the North Atlantic Ocean (Elmore et al., 2015; Thornalley, Barker, et al., 2013). The isotopic $\delta^{13}C$ signatures of benthic foraminifera south of the Nordic Seas show that the intermediate water <2 km was well ventilated during the LGM (termed Glacial North Atlantic Intermediate Water) as the Polar Front was situated south of Iceland and convection cells were active in this area (Oppo & Horowitz, 2000; Oppo & Lehman, 1993). Time periods of both low $\delta^{13}C$ and $\delta^{18}O$ could reflect formation of sea ice and brine injection particularly during HS_S and LGM, which is vital for the renewal of bottom water and deep ocean convection (Peterson, 2018; Rasmussen & Thomsen, 2004; Vidal et al., 1998).

5.4.4. Holocene

At ~9 ka, the increase in EM2 points to the intensification of overflow water at core site 905 (Figure 5), which is likely caused by the deepening and increasing strength of overflow water as is recorded in cores from the North Atlantic and the Labrador Sea (Hall et al., 2004; Hoffmann & Mertz, 1992; Kissel et al., 2013; Thornalley, Blaschek, et al., 2013). The absence of late Holocene sediments at the deep site coincides with the maximum overflow during the mid-Holocene thermal maximum (~7 ka BP; Rasmussen, Bigler, et al., 2014). The older core top AMS ^{14}C age (16,991 $\pm$ 50 years BP) at site 909 suggests that the nondeposition zone related to maximum flow speed shifted through time with increasing water depth, in line with observations by Thornalley, Barker, et al. (2013). This vertical shift might be analogous to the progressively increasing bottom current speeds during GIs as recorded in core 905. The lack of large hiatuses and/or very coarse layers during the GIs indicates that maximum bottom current speeds were not reached until the Holocene at the deep core site over the last ~55 ka. The interglacial high sea levels, enhanced convection, and overflow from the Nordic Seas cause water masses to shoal and to cascade over the crest of IFR. Similar conditions can also be expected for the previous interglacial (MIS5) and the current rising sea level needs to be taken into account as an important control on future ISOW overflow.

6. Conclusions

1. This study provides new multiproxy paleoceanographic records from the southwestern flank of the IFR, which today routes half of the ISOW overflow water from the Nordic seas to the North Atlantic Ocean.
2. The log (Ti/K) XRF records covering the time span from ~55 to 6 ka BP display distinct shifts in provenance between local basaltic sources (i.e., Iceland and Faroe Islands) and distal felsic sources comprising the British and Fennoscandian ice sheets.
3. End-member modeling of the lithogenic grain size distributions reveals three end-members, which are modified and sorted by bottom currents.
4. The proportion of EM3 and EM2 + EM1 significantly correlates to the variations in log (Ti/K) indicating that bottom current strength and provenance changes are tightly coupled together over the last ~55 to 6 kyr.
5. IRD that is irregularly dispersed in the sediment cores has a predominantly local origin from Iceland and Faroe Islands, although detrital carbonates and other rock types have been derived from distal ice sheets.
6. Heinrich-like events are characterized by the deposition of fine-grained felsic sediment originating from mouth fans, which were fed by the paleo-ice streams of the BIIS.
7. The relative sediment coarseness during the LGM at the shallow site can be linked to both strong near-bottom currents and a shoaled ISOW.
8. During GIs, dominantly Ti-rich sediments were deposited at the IFR, whereas K-rich sediments were deposited during (Heinrich) stadials. The deposition of the Ti-rich sediments cooccurs with coarse-grained lithogenic sediments due to intensified southward ISOW overflow during GIs. In contrast, the accumulation of fine-grained sediments during (Heinrich) stadials can be attributed to a weakened ISOW flow.
9. The inferred variation in bottom currents strength follows the D-O oscillation pattern during MIS-3; however, the gradual intensification is followed by an abrupt decline, which is opposite to the interstadial warming pattern recorded in Greenland ice cores. This discrepancy most likely reflects the cumulative effect of (1) near-bottom currents through the Faroe Channels and (2) overflow cascading over the IFR at the core sites 905 and 909, while paleoceanographic records at the northern entrance of the FSC are exclusively affected by water masses flowing southward through the Faroe Channels.

Acknowledgments
This study was funded and supported by the Helmholtz Research School for Ocean System Science and Technology (HOSST) program, GEOMAR. The authors are grateful to the captain and crew of RV POSEIDON cruise 457 for the recovery of cores P457-905 and P457-909. We are grateful to Nadine Gehre for technical assistance, Julien Schirrmacher for sample preparation, and Sebastian Fessler for stable isotope measurements. Maarten Prins and Lukas Jonkers are thanked for helpful discussions on grain size analysis. All data related to this article can be found online at https://doi.org/10.1594/PANGAEA.901946, the Data Publisher for Earth & Environmental Science, PANGAEA.

References

Abbott, P. M., & Davies, S. M. (2012). Volcanism and the Greenland ice-cores: The tephra record. *Earth-Science Reviews*, *115*(3), 173–191.

Andrews, J. T. (2000). Icebergs and iceberg rafted detritus (IRD) in the North Atlantic: Facts and assumptions. *Oceanography-Washington Dc-Oceanography Society*, *13*(3), 100–108.

Arnalds, O., Dagsson-Waldhauserova, P., & Olafsson, H. (2016). The Icelandic volcanic aeolian environment: Processes and impacts—A review. *Aeolian Research*, *20*, 176–195.

Arnalds, O., Ólafsson, H., & Dagsson-Waldhauserova, P. (2014). Quantification of iron-rich volcanogenic dust emissions and deposition over the ocean from Icelandic dust sources. *Biogeosciences*, *11*(23), 6623–6632. https://doi.org/10.5194/bg-11-6623-2014

Arz, H. W., Lamy, F., Ganopolski, A., Nowaczyk, N., & Pätzold, J. (2007). Dominant Northern Hemisphere climate control over millennial-scale glacial sea-level variability. *Quaternary Science Reviews*, *26*(3), 312–321.

Ballini, M., Kissel, C., Colin, C., & Richter, T. (2006). Deep-water mass source and dynamic associated with rapid climatic variations during the last glacial stage in the North Atlantic: A multiproxy investigation of the detrital fraction of deep-sea sediments. *Geochemistry, Geophysics, Geosystems*, *7*, Q02N01. https://doi.org/10.1029/2005GC001070

Barker, S., Chen, J., Gong, X., Jonkers, L., Knorr, G., & Thornalley, D. (2015). Icebergs not the trigger for North Atlantic cold events. *Nature*, *520*(7547), 333.

Beaird, N., Rhines, P., & Eriksen, C. (2013). Overflow waters at the Iceland–Faroe Ridge observed in multiyear seaglider surveys. *Journal of Physical Oceanography*, *43*(11), 2334–2351.

Blott, S. J., & Pye, K. (2001). GRADISTAT: A grain size distribution and statistics package for the analysis of unconsolidated sediments. *Earth surface processes and Landforms*, *26*(11), 1237–1248.

Boessenkool, K., Hall, I., Elderfield, H., & Yashayaev, I. (2007). North Atlantic climate and deep-ocean flow speed changes during the last 230 years. *Geophysical Research Letters*, *34*, L13614. https://doi.org/10.1029/2007GL030285

Bonanati, C., Wehrmann, H., Portnyagin, M., Hoernle, K., Mirzaloo, M., & Nürnberg, D. (2016). Tephra in marine sediment cores offshore southern Iceland: A 68,000 year record of explosive volcanism, paper presented at EGU General Assembly Conference Abstracts.

Bond, G., Heinrich, H., Broecker, W., Labeyrie, L., McManus, J., Andrews, J., et al. (1992). Evidence for massive discharges of icebergs into the North Atlantic ocean during the last glacial period. *Nature*, *360*(6401), 245.

Boulton, G., Thors, K., & Jarvis, J. (1988). Dispersal of glacially derived sediment over part of the continental shelf of south Iceland and the geometry of the resultant sediment bodies. *Marine Geology*, *83*(1-4), 193–223.

Bower, A., Furey, H., & Lozier, S. (2017). Overflow water pathways in the subpolar North Atlantic observed with deep floats, paper presented at EGU General Assembly Conference Abstracts.

Davies, S. M., Wastegård, S., Abbott, P., Barbante, C., Bigler, M., Johnsen, S. J., et al. (2010). Tracing volcanic events in the NGRIP ice-core and synchronising North Atlantic marine records during the last glacial period. *Earth and Planetary Science Letters*, *294*(1-2), 69–79.

Dokken, T. M., Nisancioglu, K. H., Li, C., Battisti, D. S., & Kissel, C. (2013). Dansgaard-Oeschger cycles: Interactions between ocean and sea ice intrinsic to the Nordic seas. *Paleoceanography*, *28*, 491–502. https://doi.org/10.1002/palo.20042

Dorn, W., & Werner, F. (1993). The contour-current flow along the southern Iceland—Faeroe Ridge as documented by its bedforms and asymmetrical channel fillings. *Sedimentary Geology*, *82*(1-4), 47–59.

Dowdeswell, J., Elverhøi, A., Andrews, J., & Hebbeln, D. (1999). Asynchronous deposition of ice-rafted layers in the Nordic seas and North Atlantic Ocean. *Nature*, *400*(6742), 348.

Elmore, A. C., Wright, J. D., & Chalk, T. B. (2015). Precession-driven changes in Iceland–Scotland Overflow Water penetration and bottom water circulation on Gardar Drift since ~200 ka. *Palaeogeography, Palaeoclimatology, Palaeoecology*, *440*, 551–563.

Ezat, M. M., Rasmussen, T. L., & Groeneveld, J. (2014). Persistent intermediate water warming during cold stadials in the southeastern Nordic seas during the past 65 ky. *Geology*, *42*(8), 663–666.

Ezat, M. M., Rasmussen, T. L., Thornalley, D. J., Olsen, J., Skinner, L. C., Hönisch, B., & Groeneveld, J. (2017). Ventilation history of Nordic Seas overflows during the last (de) glacial period revealed by species-specific benthic foraminiferal ^{14}C dates. *Paleoceanography*, *32*, 172–181. https://doi.org/10.1002/2016PA003053

Grant, K., Rohling, E., Ramsey, C. B., Cheng, H., Edwards, R., Florindo, F., et al. (2014). Sea-level variability over five glacial cycles. *Nature communications*, *5*, 5076.

Griggs, A. J., Davies, S. M., Abbott, P. M., Rasmussen, T. L., & Palmer, A. P. (2014). Optimising the use of marine tephrochronology in the North Atlantic: A detailed investigation of the Faroe Marine Ash Zones II, III and IV. *Quaternary Science Reviews*, *106*, 122–139.

Grützner, J., & Higgins, S. M. (2010). Threshold behavior of millennial scale variability in deep water hydrography inferred from a 1.1 Ma long record of sediment provenance at the southern Gardar Drift. *Paleoceanography*, *25*, PA4204. https://doi.org/10.1029/2009PA001873

Hall, I. R., Bianchi, G. G., & Evans, J. R. (2004). Centennial to millennial scale Holocene climate-deep water linkage in the North Atlantic. *Quaternary Science Reviews*, *23*(14-15), 1529–1536.

Hansen, B., & Meincke, J. (1979). Eddies and meanders in the Iceland-Faroe Ridge area. *Deep Sea Research Part A. Oceanographic Research Papers*, *26*(9).

Hansen, B., & Østerhus, S. (2000). North Atlantic–Nordic seas exchanges. *Progress in Oceanography*, *45*(2), 109–208.

Heinrich, H. (1988). Origin and consequences of cyclic ice rafting in the northeast Atlantic Ocean during the past 130,000 years. *Quaternary research*, *29*(2), 142–152.

Hodell, D. A., Channell, J. E., Curtis, J. H., Romero, O. E., & Röhl, U. (2008). Onset of "Hudson Strait" Heinrich events in the eastern North Atlantic at the end of the middle Pleistocene transition (~640 ka)? *Paleoceanography*, *23*, PA4218. https://doi.org/10.1029/2008PA001591

Hodell, D. A., Evans, H. F., Channell, J. E., & Curtis, J. H. (2010). Phase relationships of North Atlantic ice-rafted debris and surface-deep climate proxies during the last glacial period. *Quaternary Science Reviews*, *29*(27), 3875–3886.

Hoff, U., Rasmussen, T. L., Stein, R., Ezat, M. M., & Fahl, K. (2016). Sea ice and millennial-scale climate variability in the Nordic seas 90 (thinsp) kyr ago to present. *Nature Communications*, *7*.

Hoffmann, G., & Mertz, D. F. (1992). Sedimentation patterns of the Iceland-Faroe Ridge and volcanism within the Tjörnes Fracture Zone north of Iceland = Seimentationsmuster am Island-Faroer-Rücken und Vulkanismus im Bereich der Tjörnes-Bruchzone nördlich Islands: Cruise report 185/3, RV" Poseidon"(POS185/3).

Hoffmann, S. S., Dalsing, R. E., & Murphy, S. C. (2019). Sortable silt records of intermediate-depth circulation and sedimentation in the Southwest Labrador Sea since the Last Glacial Maximum. *Quaternary Science Reviews*, *206*, 99–110.

Hubbard, A., Sugden, D., Dugmore, A., Norddahl, H., & Pétursson, H. G. (2006). A modelling insight into the Icelandic Last Glacial Maximum ice sheet. *Quaternary Science Reviews*, *25*(17-18), 2283–2296.

Hughes, A. L., Gyllencreutz, R., Lohne, Ø. S., Mangerud, J., & Svendsen, J. I. (2016). The last Eurasian ice sheets—A chronological database and time-slice reconstruction, DATED-1. *Boreas*, *45*(1), 1–45.

Ingólfsson, Ó., Björck, S., Haflidason, H., & Rundgren, M. (1997). Glacial and climatic events in Iceland reflecting regional North Atlantic climatic shifts during the Pleistocene-Holocene transition. *Quaternary Science Reviews*, *16*(10), 1135–1144.

Jonkers, L. (2010). Rapid oceanographic changes associated with last glacial ice-rafting events, Vrije Universiteit and royal NIOZ, Amsterdam.

Jonkers, L., Barker, S., Hall, I. R., & Prins, M. A. (2015). Correcting for the influence of ice-rafted detritus on grain size-based paleocurrent speed estimates. *Paleoceanography*, *30*, 1347–1357. https://doi.org/10.1002/2015PA002830

Jonkers, L., Prins, M. A., Brummer, G. J. A., Konert, M., & Lougheed, B. C. (2009). Experimental insights into laser diffraction particle sizing of fine-grained sediments for use in palaeoceanography. *Sedimentology*, *56*(7), 2192–2206.

Jonkers, L., Prins, M. A., Moros, M., Weltje, G. J., Troelstra, S. R., & Brummer, G.-J. A. (2012). Temporal offsets between surface temperature, ice-rafting and bottom flow speed proxies in the glacial (MIS 3) northern North Atlantic. *Quaternary Science Reviews*, *48*, 43–53.

Keigwin, L., Jones, G., Lehman, S., & Boyle, E. (1991). Deglacial meltwater discharge, North Atlantic deep circulation, and abrupt climate change. *Journal of Geophysical Research*, *96*(C9), 16,811–16,826.

Kissel, C. (2005). Magnetic signature of rapid climatic variations in glacial North Atlantic, a review. *Comptes Rendus Geoscience*, *337*(10-11), 908–918.

Kissel, C., Laj, C., Labeyrie, L., Dokken, T., Voelker, A., & Blamart, D. (1999). Rapid climatic variations during marine isotopic stage 3: Magnetic analysis of sediments from Nordic Seas and North Atlantic. *Earth and Planetary Science Letters*, *171*(3), 489–502.

Kissel, C., Van Toer, A., Laj, C., Cortijo, E., & Michel, E. (2013). Variations in the strength of the North Atlantic bottom water during Holocene. *Earth and Planetary Science Letters*, *369*, 248–259.

Kuijpers, A., Hansen, B., Hühnerbach, V., Larsen, B., Nielsen, T., & Werner, F. (2002). Norwegian Sea overflow through the Faroe–Shetland gateway as documented by its bedforms. *Marine Geology*, *188*(1), 147–164.

Kuijpers, A., & Nielsen, T. (2016). Near-bottom current speed maxima in North Atlantic contourite environments inferred from current-induced bedforms and other seabed evidence. *Marine Geology*, *378*, 230–236.

Kuijpers, A., Troelstra, S., Wisse, M., Nielsen, S. H., & Van Weering, T. (1998). Norwegian Sea overflow variability and NE Atlantic surface hydrography during the past 150,000 years. *Marine Geology*, *152*(1), 75–99.

Lamy, F., Arz, H. W., Kilian, R., Lange, C. B., Lembke-Jene, L., Wengler, M., et al. (2015). Glacial reduction and millennial-scale variations in Drake Passage throughflow. *Proceedings of the National Academy of Sciences*, *112*(44), 13,496–13,501.

Manighetti, B., & McCave, I. (1995). Late glacial and Holocene palaeocurrents around Rockall Bank, NE Atlantic Ocean. *Paleoceanography*, *10*(3), 611–626.

Maslin, M. (1995). Changes in North Atlantic deep water formation associated with the Heinrich events. *Naturwissenschaften*, *82*(7), 330–333.

Masson, D., Wynn, R., & Bett, B. (2004). Sedimentary environment of the Faroe-Shetland and Faroe Bank Channels, north-east Atlantic, and the use of bedforms as indicators of bottom current velocity in the deep ocean. *Sedimentology*, *51*(6), 1207–1241.

McCave, I., & Andrews, J. (2019). Distinguishing current effects in sediments delivered to the ocean by ice. I. Principles, methods and examples. *Quaternary Science Reviews*, *212*, 92–107.

McCave, I., & Hall, I. R. (2006). Size sorting in marine muds: Processes, pitfalls, and prospects for paleoflow-speed proxies. *Geochemistry, Geophysics, Geosystems*, *7*, Q10N05. https://doi.org/10.1029/2006GC001284

McCave, I., Thornalley, D., & Hall, I. (2017). Relation of sortable silt grain-size to deep-sea current speeds: Calibration of the "Mud Current Meter,". *Deep Sea Research Part I: Oceanographic Research Papers*, *127*, 1–12.

Navrátil, T., Hladil, J., Strnad, L., Koptíková, L., & Skála, R. (2013). Volcanic ash particulate matter from the 2010 Eyjafjallajökull eruption in dust deposition at Prague, central Europe. *Aeolian Research*, *9*, 191–202.

Nørgaard-Pedersen, N., Spielhagen, R. F., Erlenkeuser, H., Grootes, P. M., Heinemeier, J., & Knies, J. (2003). Arctic Ocean during the Last Glacial Maximum: Atlantic and polar domains of surface water mass distribution and ice cover. *Paleoceanography*, *18*(3), 1063. https://doi.org/10.1029/2002PA000781

Nürnberg, D., Dethleff, D., Tiedemann, R., Kaiser, A., & Gorbarenko, S. A. (2011). Okhotsk Sea ice coverage and Kamchatka glaciation over the last 350 ka—Evidence from ice-rafted debris and planktonic $\delta^{18}O$. *Palaeogeography, Palaeoclimatology, Palaeoecology*, *310*(3-4), 191–205.

Olsen, J., Rasmussen, T. L., & Reimer, P. J. (2014). North Atlantic marine radiocarbon reservoir ages through Heinrich event H4: A new method for marine age model construction. *Geological Society, London, Special Publications*, *398*.

Oppo, D., & Lehman, S. (1993). Mid-depth circulation of the subpolar North Atlantic during the last glacial maximum. *Science*, *259*(5098), 1148–1152.

Oppo, D. W., & Horowitz, M. (2000). Glacial deep water geometry: South Atlantic benthic foraminiferal Cd/Ca and $\delta^{13}C$ evidence. *Paleoceanography*, *15*(2), 147–160.

Østerhus, S., Turrell, W. R., Hansen, B., Lundberg, P., & Buch, E. (2001). Observed transport estimates between the North Atlantic and the Arctic Mediterranean in the Iceland–Scotland region. *Polar Research*, *20*(2), 169–175.

Ostmann, A., Schnurr, S., & Arbizu, P. M. (2014). Marine environment around Iceland: Hydrography, sediments and first predictive models of Icelandic deep-sea sediment characteristics. *Polish Polar Research*, *35*(2), 151–176.

Paterson, G. A., & Heslop, D. (2015). New methods for unmixing sediment grain size data. *Geochemistry, Geophysics, Geosystems*, *16*, 4494–4506. https://doi.org/10.1002/2015GC006070

Patton, H., Hubbard, A., Andreassen, K., Auriac, A., Whitehouse, P. L., Stroeven, A. P., et al. (2017). Deglaciation of the Eurasian ice sheet complex. *Quaternary Science Reviews*, *169*, 148–172.

Peck, V., Hall, I., Zahn, R., Elderfield, H., Grousset, F., Hemming, S., & Scourse, J. (2006). High resolution evidence for linkages between NW European ice sheet instability and Atlantic Meridional Overturning Circulation. *Earth and Planetary Science Letters*, *243*(3-4), 476–488.

Peterson, A. K. (2018). Observations of brine plumes below melting Arctic sea ice. *Ocean Science*, *14*(1), 127–138.

Praetorius, S. K., McManus, J. F., Oppo, D. W., & Curry, W. B. (2008). Episodic reductions in bottom-water currents since the last ice age. *Nature Geoscience*, *1*(7), 449–452.

Prins, M., Bouwer, L., Beets, C. J., Troelstra, S. R., Weltje, G. J., Kruk, R. W., et al. (2002). Ocean circulation and iceberg discharge in the glacial North Atlantic: Inferences from unmixing of sediment size distributions. *Geology*, *30*(6), 555–558.

Prins, M., Troelstra, S., Kruk, R., Van Der Borg, K., De Jong, A., & Weltje, G. J. (2001). The late Quaternary sedimentary record of Reykjanes Ridge, north Atlantic. *Radiocarbon*, *43*(2B), 939–947.

Prins, M., & Weltje, G-J. (1999). End-member modeling of siliciclastic grain-size distributions: The late Quaternary record of eolian and fluvial sediment supply to the Arabian Sea and its paleoclimatic significance.

Puteanus, D., & Werner, F. (1990). Bericht über Reise Nr. 158 (POS158) des FS Poseidon in das Seegebiet um Island = Report on cruise 158 of RV Poseidon N and SE of Iceland.

Rahmstorf, S. (2002). Ocean circulation and climate during the past 120,000 years. *Nature*, *419*(6903), 207.

Rasmussen, S., Bigler, M., Blockley, S., Blunier, T., Buchardt, S., Clausen, H., et al. (2014). A stratigraphic framework for abrupt climatic changes during the Last Glacial period based on three synchronized Greenland ice-core records: Refining and extending the INTIMATE event stratigraphy. *Quaternary Science Reviews*, *106*, 14–28.

Rasmussen, T. L., & Thomsen, E. (2004). The role of the North Atlantic Drift in the millennial timescale glacial climate fluctuations. *Palaeogeography, Palaeoclimatology, Palaeoecology*, *210*(1), 101–116.

Rasmussen, T. L., Thomsen, E., Labeyrie, L., & van Weering, T. C. (1996). Circulation changes in the Faeroe-Shetland Channel correlating with cold events during the last glacial period (58–10 ka). *Geology*, *24*(10), 937–940.

Rasmussen, T. L., Thomsen, E., & Moros, M. (2016). North Atlantic warming during Dansgaard-Oeschger events synchronous with Antarctic warming and out-of-phase with Greenland climate. *Scientific reports*, *6*, 20,535.

Rasmussen, T. L., Thomsen, E., Skirbekk, K., Ślubowska-Woldengen, M., Kristensen, D. K., & Koç, N. (2014). Spatial and temporal distribution of Holocene temperature maxima in the northern Nordic seas: Interplay of Atlantic-, Arctic- and polar water masses. *Quaternary Science Reviews*, *92*, 280–291.

Rasmussen, T. L., Thomsen, E., & Van Weering, T. C. (1998). Cyclic sedimentation on the Faeroe Drift 53-10 ka BP related to climatic variations. *Geological Society, London, Special Publications*, *129*(1), 255–267.

Rasmussen, T. L., Thomsen, E., Weering, T. C., & Labeyrie, L. (1996). Rapid changes in surface and deep water conditions at the Faeroe Margin during the last 58,000 years. *Paleoceanography*, *11*(6), 757–771.

Rebesco, M., Hernández-Molina, F. J., Van Rooij, D., & Wåhlin, A. (2014). Contourites and associated sediments controlled by deep-water circulation processes: State-of-the-art and future considerations. *Marine Geology*, *352*, 111–154.

Reimer, P. J., Bard, E., Bayliss, A., Beck, J. W., Blackwell, P. G., Ramsey, C. B., et al. (2013). IntCal13 and Marine13 radiocarbon age calibration curves 0–50,000 years cal BP. *Radiocarbon*, *55*(4), 1869–1887.

Richter, T. O., Van der Gaast, S., Koster, B., Vaars, A., Gieles, R., de Stigter, H. C., et al. (2006). The Avaatech XRF Core Scanner: Technical description and applications to NE Atlantic sediments. *Geological Society, London, Special Publications*, *267*(1), 39–50.

Sarnthein, M., Jansen, E., Weinelt, M., Arnold, M., Duplessy, J. C., Erlenkeuser, H., et al. (1995). Variations in Atlantic surface ocean paleoceanography, 50°-80°N: A time-slice record of the last 30,000 years. *Paleoceanography*, *10*(6), 1063–1094.

Schneider, R., Price, B., Müller, P., Kroon, D., & Alexander, I. (1997). Monsoon related variations in Zaire (Congo) sediment load and influence of fluvial silicate supply on marine productivity in the east equatorial Atlantic during the last 200,000 years. *Paleoceanography*, *12*(3), 463–481.

Scholle, P. A., Bebout, D. G., & Moore, C. H. (1983). Carbonate depositional environments: AAPG Memoir 33, AAPG.

Scholle, P. A., Hsu, K., & Jenkyns, H. (1974). Diagenesis of Upper Cretaceous chalks from England, Northern Ireland and the North Sea. In K. J. Hsü, & H. C. Jenkyns (Eds.), *Pelagic sediments: on land and under the sea* (pp. 177–210). https://doi.org/10.1002/9781444304855

Scourse, J. D., Haapaniemi, A. I., Colmenero-Hidalgo, E., Peck, V. L., Hall, I. R., Austin, W. E., et al. (2009). Growth, dynamics and deglaciation of the last British–Irish ice sheet: The deep-sea ice-rafted detritus record. *Quaternary Science Reviews*, *28*(27-28), 3066–3084.

Seidov, D., & Prien, R. (1996). A coarse resolution North Atlantic ocean circulation model: An intercomparison study with a paleoceanographic example, paper presented at Annales Geophysicae.

Snowball, I., & Moros, M. (2003). Saw-tooth pattern of North Atlantic current speed during Dansgaard-Oeschger cycles revealed by the magnetic grain size of Reykjanes Ridge sediments at 59 N. *Paleoceanography*, *18*(2), 1026. https://doi.org/10.1029/2001PA000732

Svensson, A., Andersen, K. K., Bigler, M., Clausen, H. B., Dahl-Jensen, D., Davies, S., et al. (2008). A 60 000 year Greenland stratigraphic ice core chronology. *Climate of the Past*, *4*(1), 47–57.

Talma, A., & Vogel, J. C. (1993). A simplified approach to calibrating ^{14}C dates. *Radiocarbon*, *35*(2), 317–322.

Thornalley, D. J., Barker, S., Becker, J., Hall, I. R., & Knorr, G. (2013). Abrupt changes in deep Atlantic circulation during the transition to full glacial conditions. *Paleoceanography*, *28*, 253–262. https://doi.org/10.1002/palo.20025

Thornalley, D. J., Blaschek, M., Davies, F. J., Praetorius, S., Oppo, D. W., McManus, J. F., et al. (2013). Long-term variations in Iceland–Scotland overflow strength during the Holocene. *Climate of the Past*, *9*(5), 2073–2084.

Van Hateren, J., Prins, M., & van Balen, R. (2018). On the genetically meaningful decomposition of grain-size distributions: A comparison of different end-member modelling algorithms. *Sedimentary geology*, *375*, 49–71.

Veres, D., Bazin, L., Landais, A., Kele, H. T. M., Lemieux-Dudon, B., Parrenin, F., et al. (2013). The Antarctic ice core chronology (AICC2012): An optimized multi-parameter and multi-site dating approach for the last 120 thousand years. *Climate of the Past*, *9*(4), 1733–1748.

Vidal, L., Labeyrie, L., & Weering, T. V. (1998). Benthic δ^{18}O records in the North Atlantic over the last glacial period (60–10 kyr): Evidence for brine formation. *Paleoceanography and Paleoclimatology*, *13*(3), 245–251.

Voelker, A. H., Grootes, P. M., Nadeau, M.-J., & Sarnthein, M. (2000). Radiocarbon levels in the Iceland Sea from 25–53 kyr and their link to the Earth's magnetic field intensity. *Radiocarbon*, *42*(3), 437–452.

Waelbroeck, C., Labeyrie, L., Michel, E., Duplessy, J. C., McManus, J., Lambeck, K., et al. (2002). Sea-level and deep water temperature changes derived from benthic foraminifera isotopic records. *Quaternary Science Reviews*, *21*(1-3), 295–305.

Wastegård, S., & Rasmussen, T. L. (2001). New tephra horizons from Oxygen Isotope Stage 5 in the North Atlantic: Correlation potential for terrestrial, marine and ice-core archives. *Quaternary Science Reviews*, *20*(15), 1587–1593.

Weltje, G. J., & Tjallingii, R. (2008). Calibration of XRF core scanners for quantitative geochemical logging of sediment cores: Theory and application. *Earth and Planetary Science Letters*, *274*(3), 423–438.

Werner, R., & Nürnberg, D. (2014). RV POSEIDON Fahrtbericht/Cruise Report P457 (POS457): Iceland hazards; volcanic risks from Iceland and climate change: The late Quaternary to anthropogene development, Reykjavík/Iceland–Galway/Ireland, 7.-22. August 2013.